3788 J. Phys. Chem. A 2001, 105, 3788−3795

Raman Spectroscopy of the Reaction of Sodium Chloride with Nitric Acid: Sodium Nitrate Growth and Effect of Water Exposure

Christopher D. Zangmeister and Jeanne E. Pemberton*

Department of Chemistry, University of Arizona, Tucson, Arizona 85721

Received: September 18, 2000; In Final Form: January 24, 2001

The reaction of powdered NaCl with HNO_3 was studied using Raman spectroscopy. $NaNO_3$ growth was monitored as a function of HNO_3 exposure in a flow cell. Mode-specific changes in the NO_3^- vibrational mode intensities with HNO_3 exposure suggest a rearrangement of the $NaNO_3$ film with coverage. In the absence of H_2O, intensities of $NaNO_3$ bands increase with HNO_3 exposure until a capping layer of $NaNO_3$ forms. The capping layer prevents subsequent HNO_3 from reacting with the underlying NaCl. H_2O exposure of $NaNO_3$-capped NaCl results in hydration of the surface to form an aqueous solution containing $NaNO_3$ and NaCl. Further exposure results in the formation of a thicker surface-adsorbed H_2O layer that is consistent with an aqueous $NaNO_3$ and NaCl solution. Upon exposure of hydrated NaCl to HNO_3, molecular HNO_3 and solid-state $NaNO_3$ are observed in the thin H_2O film.

Introduction

The evaporation of sea-salt aerosols is estimated to release $\sim 10^{12}$ kg of NaCl to the troposphere per year.[1] Many studies have shown a significant chloride deficit in these particles (30−80%) when compared to bulk seawater.[2−5] This deficit has been attributed to reactions with inorganic nitrogen and sulfur oxide species.[6−17] The reaction of particulate NaCl with these compounds is an important link between a natural process, the evaporation of sea salt aerosols, and an anthropogenic process, the formation of inorganic nitrogen and sulfur oxide species derived from the burning of fossil fuels.

Ultimately, these reactions generate the corresponding sodium salt and volatile chlorine compounds.[6−17] Volatile atmospheric chlorine, such as reservoir HCl and $ClONO_2$, have been implicated in such processes as the destruction of stratospheric ozone and the initiation of free radical reactions of gas-phase organics.[18]

One extensively studied reaction is that of NaCl with HNO_3

$$NaCl(s) + HNO_3(g) \rightleftharpoons NaNO_3(s) + HCl(g) \qquad (1)$$

This reaction is inherently heterogeneous. Many studies on this system have been reported in which the loss of gaseous reactants or the production of gaseous products were monitored.[10−12,17] Far fewer studies[14−16] have focused on the surface chemistry involved in this reaction. To illustrate the importance of the nature of the surface in this reaction, one needs only to consider the variation in reaction probability, γ (number of reactions per surface collision event), elucidated for this reaction on differently prepared surfaces using mass spectrometry.[10,11,14,17] On well-ordered NaCl (100), γ values of 4×10^{-4} have been obtained. In contrast, on defective surfaces such as powdered NaCl, γ increases to $(1.3-5.5) \times 10^{-2}$.[10,11,14,17] γ values spanning a range of approximately 2 orders of magnitude clearly indicate the important role played by the surface in this reaction. On this basis, further surface-based investigations are warranted.

Previous surface studies of this reaction have been undertaken using X-ray photoelectron spectroscopy (XPS), transmission electron microscopy (TEM), diffuse reflectance FTIR (DRIFTS), and atomic force microscopy (AFM). These studies have demonstrated the formation of a 1−2 monolayer uniform passivating layer of $NaNO_3$ upon initial exposure to dry HNO_3.[14−17,19] This layer inhibits further reaction by prohibiting access of HNO_3 to the underlying NaCl. Subsequent H_2O exposure of the passivating layer results in its rearrangement to crystallites of $NaNO_3$ on the NaCl surface. This process has been shown in this laboratory to proceed through transient mobile features on the hydrated NaCl surface using AFM in real time.[19] Although these features are presumed to be $NaNO_3$, no definitive data are in hand that unequivocally support this assignment. Thus, further studies are needed to completely elucidate the mechanistic pathway whereby this transformation occurs.

Toward this end, the effort reported here was undertaken in an attempt to better define the surface chemistry associated with the reaction of NaCl with HNO_3. Raman spectroscopy was chosen for this task on the basis of its molecular specificity, access to the entire frequency region wherein vibrations of these inorganic species are observed, and its relative freedom from spectral interference by water.

Experimental Section

Instrumentation. Raman spectra were acquired using 125 mW of 514.5 nm radiation from an Ar^+ laser (Spectra Physics Model 164). A Minolta f/1.2 camera lens was used to collect scattered radiation at 90° with respect to the incident radiation. A Spex 1877 Triplemate spectrometer equipped with a 600gr/mm grating in the filter stage and a 1200 gr/mm grating in the spectrograph were used. The entrance slit of the spectrograph was set at 0.5 mm, the filter stage slit was set at 7.0 mm, and the spectrograph stage was 75 μm. A Princeton Instruments RTE-1100-PB thinned, back-illuminated CCD camera of 1100 × 330 pixel format and cooled to −90 °C was used for detection.

---

* Corresponding author. E-mail: pembertn@u.arizona.edu. Tel.: 520-621-8245. Fax: 520-621-8248.

10.1021/jp003374n CCC: $20.00

Spectra were calibrated using Ar^+ plasma lines. Curve fitting of Raman spectra was performed using the Grams 386 (Galactic Industries) program. Peak positions and widths were not restrained and were fit with a variable Gaussian−Lorentzian peak shape.

Scanning electron microscopy (SEM) images were acquired on a Hitachi S-2460N SEM instrument with an accelerating voltage of 20 kV. To ensure conductivity, all samples were coated with Au prior to analysis.

Materials. NaCl (Aldrich, >99.5%) was recrystallized in 75:25 H_2O:ethanol solution and filtered. The collected solid was dried and stored at 550 °C to remove surface-bound H_2O. Measures were taken to ensure that contact with ambient air was minimized.

Scanning electron microscopy of the recrystallized NaCl crystals used here shows them to be well-defined cubes with ~7 μm sides and angled corners. The surface crystallinity of NaCl is known to be influenced by the conditions under which precipitation is initiated.[20−22] The (100) crystal face is the lowest-energy surface and is preferred upon recrystallization.[20−22] Other low index faces are possible under conditions of fast precipitation and/or upon the addition of organic solvents to the recrystallization solution. On the basis of the SEM of the NaCl used here, the cube faces consist of the (100) face with corners cut at 45° resulting in (111) faces. The micrographs indicate that ~75% of these surfaces are NaCl (100), with the remaining ~25% as NaCl (111).

NaCl surfaces prepared by precipitation are relatively nonporous. Previous work has shown that the geometric surface area of NaCl powders is in good agreement with BET isotherm determinations.[8−10] If perfect 7 μm cubes are assumed, the geometric surface area of the powders used here is $\sim 4 \times 10^3$ cm^2/g. Therefore, each sample for Raman spectroscopy consisted of 750 ± 50 cm^2 of surface area, or $\sim 1.2 \times 10^{-7}$ moles of exposed surface NaCl.

Dry HNO_3 vapor was prepared with a 1:2 (v/v) mixture of HNO_3 (Aldrich, 99%): H_2SO_4 (Aldrich, >98%).[3] $NaNO_3$-capped NaCl was produced by exposing dry, recrystallized NaCl to dry HNO_3 in a sealed container for 12 h.

Procedures. Raman spectra were acquired using a flow cell built in-house. Approximately 0.2 g of NaCl powder was placed at the end of a Pyrex flow tube, and reactant headspace gas (HNO_3 or H_2O) was pumped through at $\sim 10^{-6}$ moles s^{-1}. (At this flow rate, the system may not be at equilibrium.) The rate of gas flow was determined after each experiment by measuring the time required to evacuate a known volume filled with H_2O.

The glass cell was positioned in front of the collection optics of the spectrometer, allowing the same sample volume to be interrogated throughout the experiment. Spectra were acquired as a function of time. Gas flow was stopped during spectral acquisition to minimize exposure of the powder to the headspace gas during spectral acquisition (0.5−2 min/spectrum). The gas flow rate (1.1−1.3 mL s^{-1}) was much lower than the headspace volume flow (~75 mL). It was assumed that the residence time of gas (60 s) in the flow cell was sufficient to saturate the flow gas. At these flow rates, 6×10^{-6} moles of HNO_3 s^{-1} (3.6×10^{18} molecules cm^{-3}) and 1×10^{-5} moles of H_2O s^{-1} (6.0×10^{18} molecules cm^{-3}) were delivered to the powder. When exposure at these flow rates occurs for a set time, exposure amounts can be determined in moles. Once normalized for surface area of the NaCl, exposure values can be determined and are reported throughout in units of moles per square centimeter.

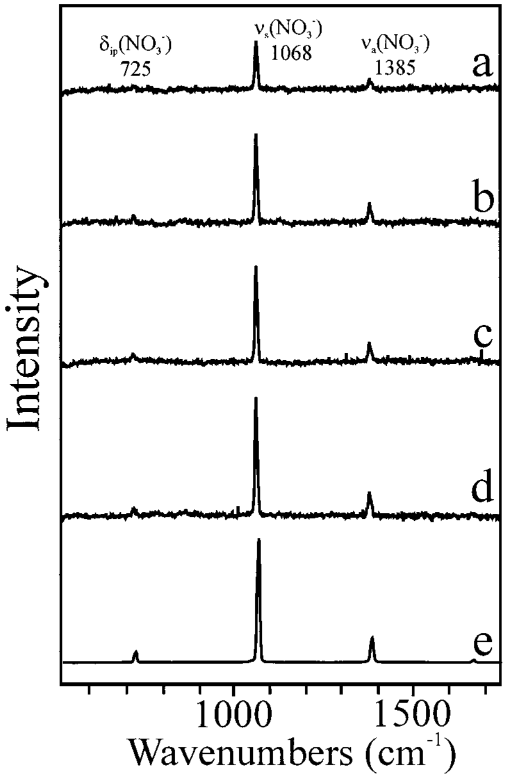

Figure 1. Raman spectra from NaCl powder after exposure to dry gaseous HNO_3: (a) $\sim 1.0 \times 10^{-7}$, (b) $\sim 3.4 \times 10^{-7}$, (c) $\sim 1.0 \times 10^{-6}$, and (d) $\sim 2.5 \times 10^{-6}$ moles HNO_3 cm^{-2} and (e) bulk crystalline $NaNO_3$.

Results & Discussion

$NaNO_3$ Passivating Layer Formation. Previous studies have demonstrated the formation of a passivating layer of amorphous $NaNO_3$ upon exposure of NaCl to dry HNO_3.[14−17] AFM studies previously reported from this laboratory confirm the amorphous nature of this layer.[19] Given the extreme sensitivity of the vibrational spectroscopy of oxyanions such as NO_3^- to chemical environment, a manifestation of the amorphous nature of this $NaNO_3$ was expected in the Raman spectral response. Figure 1 shows Raman spectra of the formation of this $NaNO_3$ layer at various stages during exposure of NaCl to a flowing stream of HNO_3 of 8×10^{-9} moles cm^{-2} s^{-1} (Figure 1a−d) and a spectrum of bulk crystalline $NaNO_3$ (Figure 1e) for comparison. As shown in Figure 1a, $NaNO_3$ can be detected after exposure to as little as $\sim 1.0 \times 10^{-7}$ moles of HNO_3 vapor per cm^2 of NaCl surface area. The free NO_3^- ion is a member of the D_{3h} point group, with three Raman-active vibrational modes in bulk $NaNO_3$: the $\delta_{ip}(NO_3^-)$ at 725 cm^{-1}, the $\nu_s(NO_3^-)$ at 1068 cm^{-1}, and the $\nu_a(NO_3^-)$ at 1385 cm^{-1}. All three bands are clearly observed in Figure 1a, and contrary to expectations, the peak frequencies for this amorphous $NaNO_3$ are identical to those of crystalline $NaNO_3$. As shown by the spectra in Figure 1b−d, the $NaNO_3$ signals continue to increase with HNO_3 exposure up to 2.5×10^{-6} moles cm^{-2}; however, subsequent exposure produces no further increase in $NaNO_3$ intensities, indicating completion of the passivating layer.

Upon closer inspection of these spectra, subtle coverage-dependent changes in the vibrational response of the amorphous $NaNO_3$ emerge despite the similarity in peak frequencies with crystalline $NaNO_3$. Figure 2a shows plots of the intensities of two NO_3^- modes, the $\nu_s(NO_3^-)$ at 1068 cm^{-1}, and the $\delta_{ip}(NO_3^-)$ at 725 cm^{-1} as a function of HNO_3 exposure. The $\nu_s(NO_3^-)$ response with coverage is well-behaved and can be fit to the Langmuir isotherm represented by the solid line in Figure 2a.

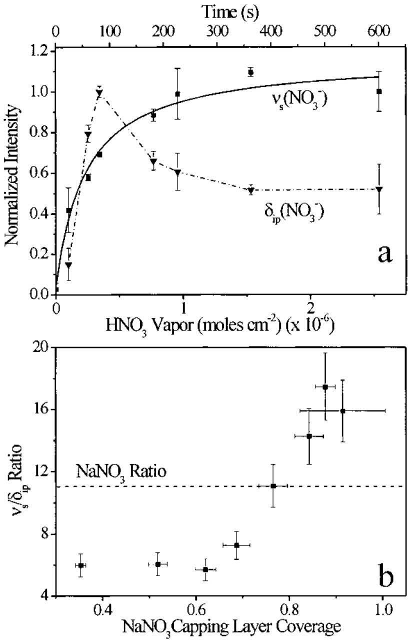

Figure 2. (a) Normalized intensity of $\nu_s(NO_3^-)$ and $\delta_{ip}(NO_3^-)$ as a function of HNO_3 exposure; (b) intensity ratio of $\nu_s(NO_3^-)$ to $\delta_{ip}(NO_3^-)$ as a function of passivating layer fractional surface coverage.

In contrast, the $\delta_{ip}(NO_3^-)$ response is unusual, exhibiting first an increase and then a decrease during formation of the passivating layer.

The well-behaved response of the $\nu_s(NO_3^-)$ allows estimation of fractional surface coverage by the passivating layer, assuming that the layer is completed as the $\nu_s(NO_3^-)$ intensity levels off. Using this estimate of surface coverage, a plot of the peak intensity ratio of the $\nu_s(NO_3^-)$ to the $\delta_{ip}(NO_3^-)$ as a function of surface coverage is shown in Figure 2b. This intensity ratio changes significantly as a function of $NaNO_3$ coverage despite the consistency of the peak frequencies. Specifically, this ratio changes by a factor of ~3 as a function of coverage, increasing from 6:1 for coverages less than ~0.6 ML to 18:1 upon completion of the passivating layer. In bulk $NaNO_3$, this ratio is ca. 11:1; thus, the observed values span a range from less than to greater than that of crystalline $NaNO_3$.

The spectral changes indicate different NO_3^- environments that change systematically with coverage of the amorphous layer. To rationalize these observations, one must consider the nature of the vibrational motions of each mode in the context of the mechanism of the passivating layer formation. These two vibrational modes interrogate different motions of the NO_3^- ion. The $\nu_s(NO_3^-)$ represents a symmetric breathing motion of all atoms in the plane of the ion while the angles between the N—O bonds remain constant. In contrast, the $\delta_{ip}(NO_3^-)$ represents bending of the ion through alteration of the N—O bond angles even though all N—O bonds remain within the plane of the ion. To understand how these different motions might be impacted by the chemical environment of the $NaNO_3$ passivating layer as it forms, one must know the mechanism by which this layer forms. The atomic motions corresponding to these vibrational modes and two possible extreme surface orientations of NO_3^- are shown in Figure 3.

The growth of this passivating layer has been imaged as a function of static HNO_3 exposure in previous AFM studies from this laboratory.[19] During the initial stages of growth, the images show growth of $NaNO_3$ on step edges followed by growth on terrace sites. If it is assumed that step edge growth is complete prior to the coverage at which Raman spectra can first be observed, then analysis of the changes in intensity ratios must only involve $NaNO_3$ growth on the terraces. Preliminary modeling of this reaction on NaCl (100) terraces has been undertaken using force field energy minimization calculations available in version 2.0 of Cerius^2. Although admittedly a highly simplistic treatment, these preliminary calculations were undertaken using the Dreiding 2.11 force field.[23] This force field is regarded as the universal force field in the prediction of the structure and dynamics of organic and main-group inorganic molecules and has recently been applied to predict the orientation of molecules on surfaces.[24] For the studies reported here, these calculations are viewed only as a starting point; future efforts will utilize sophisticated force fields more applicable to these ionic surfaces.

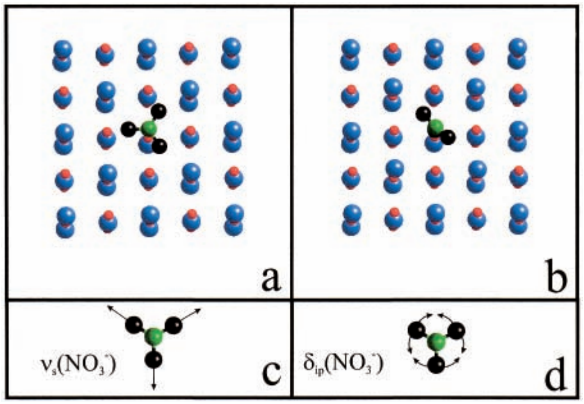

Figure 3. (a) Horizontal orientation of NO_3^- over Cl^- surface vacancy; (b) vertical orientation of NO_3^- inserted into Cl^- surface vacancy; (c) atomic motions involved in $\nu_s(NO_3^-)$; (d) atomic motions involved in $\delta_{ip}(NO_3^-)$.

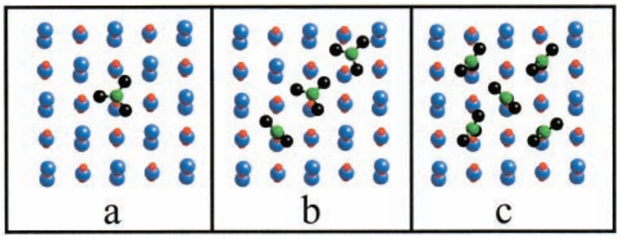

Figure 4. Energy-minimized orientations of NO_3^- for (a) one Cl^- surface vacancy, (b) three Cl^- surface vacancies, and (c) five Cl^- surface vacancies.

In these calculations, a 5 × 5 × 3 lattice of NaCl was created, and the bottom layer was fixed to the lattice spacing of crystalline NaCl. The other two layers of NaCl and the orientation and position of NO_3^- were allowed to change until the system converged. On NaCl (100) terraces, the growth of the $NaNO_3$ layer is envisioned to start through the production of HCl at isolated sites on NaCl leaving Cl^--deficient surface defects. The calculations of the initial stages of this reaction suggest that the NO_3^- species interact at these defects in an orientation in which the ion plane is parallel to the surface as shown in Figure 4a. In this orientation, the various components of the polarizability tensor for the $\nu_s(NO_3^-)$ and $\delta_{ip}(NO_3^-)$ modes are expected to be perturbed from their values in crystalline $NaNO_3$ due to the proximity to the NaCl surface. These perturbations are manifest as an intensity ratio for these modes lower than that observed in the bulk crystalline solid.

As the surface reaction proceeds and more of the surface Cl^- is removed as HCl, an increasing number of surface NO_3^- species undergo a systematic change in orientation with coverage, first to a mixed-mode orientation as shown in Figure 4b

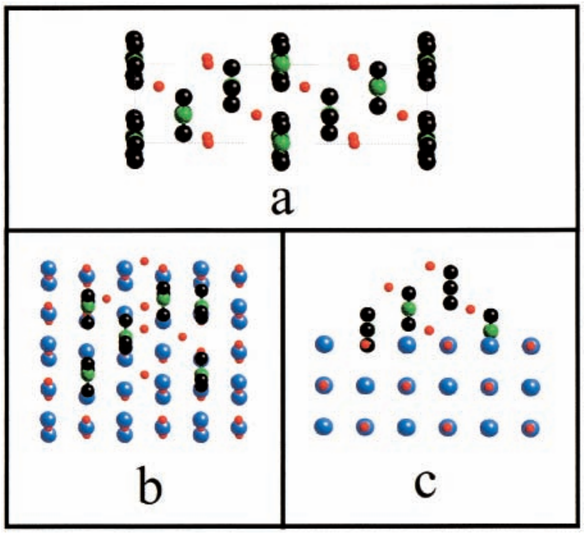

Figure 5. (a) Crystal structure of bulk $NaNO_3$; (b) energy-minimized top view of NaCl surface upon contact with bulk $NaNO_3$; (c) side view of panel b.

and finally to a perfectly vertical orientation as shown in Figure 4c. This reorientation produces a commensurate change in Raman intensity ratio of these vibrational modes, since the electronic environment dictating the polarizability tensor components is systematically altered. In the vertical NO_3^- orientation, one O atom of the ion is imbedded into the Cl vacancy on the surface such that the center of the NO_3^- plane is positioned adjacent to the Na^+ in the upper atomic layer of the NaCl surface. The interactions produced by this arrangement apparently decrease the intensity of the $\delta_{ip}(NO_3^-)$ more than the $\nu_s(NO_3^-)$ based on the increase of this ratio (see Figure 2.)

Further evidence in support of this vertical NO_3^- arrangement in the final passivating layer comes from consideration of the crystal structure of bulk $NaNO_3$. As shown by the picture in Figure 5a, the structural motif of this salt is one in which the Na^+ and NO_3^- exist in a linear arrangement in the $X-Z$ plane. Thus, one concludes that $NaNO_3$ in the passivating layer has a structure as shown schematically in Figure 5b,c. The amorphous nature of the passivating layer is rationalized by the fact that the $Na^+-NO_3^-$ distance in bulk $NaNO_3$ is 3.24 Å but the $Na^+ - Cl^-$ distance in NaCl is only 2.75 Å, ~15% smaller. Thus, the $NaNO_3$ accommodated by the NaCl (100) surface cannot achieve its equilibrium crystalline spacing and, therefore, forms an amorphous state in which some of the $NaNO_3$ is displaced in the z-direction as shown by the side view in Figure 5c.

The kinetics of passivating layer formation can be extracted from the Raman band intensities as a function of HNO_3 exposure. Referring back to the plot of the $\nu_s(NO_3^-)$ intensity as a function of HNO_3 exposure shown in Figure 2a, one sees that the intensity levels off after ~350 s (1.6×10^{-6} moles cm^{-2}) of HNO_3 exposure. Indeed, the solid line in Figure 2a is a Langmuir fit to these data, showing the well-behaved nature of this response. Previous work has shown this reaction to be pseudo-first order in HNO_3.[10-13,16,17] The linear nature of a plot of $\ln\{1 - I[\nu_s(NO_3^-)]\}$ as a function of HNO_3 exposure shown in Figure 6 verifies this reaction order. The rate constant determined from the slope of this plot is $(1.18 \pm 0.12) \times 10^{-2}$ $mole^{-1}$.

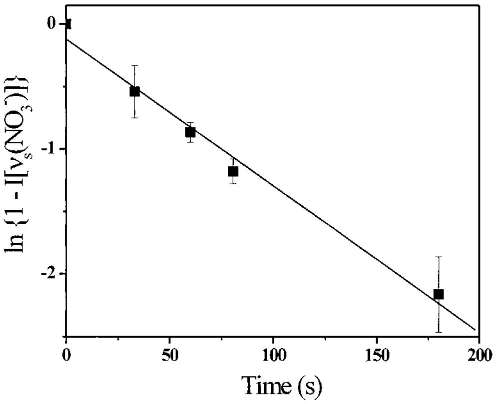

Figure 6. First-order rate plot ($\ln\{1-[\nu_s(NO_3^-)]\}$ vs time) for the initial reaction of dry HNO_3 with NaCl.

Reactions of a gas with a solid can also be described in terms of a reaction probability, γ, or the number of reactions per surface collision.[10-13,16,17] Determination of γ requires knowledge of the collision rate, C, which can be determined from the following relationship:

$$C = A_{surf} P_{gas}/[RT/(2\pi M)]^{1/2} \tag{2}$$

where A_{surf} is the surface area of the powder, P_{gas} is the vapor pressure of HNO_3 at STP (62.8 Torr), and M is the molecular weight of HNO_3. With C in hand, one can calculate γ from

$$\gamma = \frac{d[NO_3^-]}{dt}\frac{1}{C} \tag{3}$$

On the basis of our Raman spectral data, γ was determined to be $(5.9 \pm 0.8) \times 10^{-2}$. This result is the first spectroscopic elucidation of γ and is slightly larger than previously published values for powdered NaCl determined on the basis of HCl detection.[10-13,16,17] It can be argued that the direct detection of the solid-phase product is preferable to gas-phase HCl monitoring for the determination of γ because it is not hampered by the retention of HCl through dissolution in surface H_2O that could potentially reduce the measured value of γ.

Variations in γ are expected due to the large number of variables (e.g., surface porosity, surface morphology, surface crystal structure, surface adsorbed H_2O, number of surface defect sites, sample history) that could affect the kinetics of this system. The large variation in γ between single crystal and powdered samples suggests that the kinetics of this reaction may depend on the presence of active surface sites. To understand the factors that govern the production of surface $NaNO_3$, this reaction can be considered as a two-step process, as shown below:[16]

$$HNO_3\,(g) \underset{k_{-1}}{\overset{k_1}{\rightleftharpoons}} HNO_3\,(ads) \tag{4}$$

$$HNO_3\,(ads) + NaCl\,(s) \underset{k_{-2}}{\overset{k_2}{\rightleftharpoons}} NaNO_3\,(s) + HCl\,(g) \tag{5}$$

In this model, the reaction is separated into the adsorption/desorption of HNO_3 on NaCl (k_1, k_{-1}) and the reaction of adsorbed HNO_3 at a NaCl active site (k_2, k_{-2}). The sticking (adsorption) coefficient for HNO_3 on NaCl has yet to be determined. Factors that govern this parameter may be surface crystal structure, step edge density, and H_2O coverage. Since the flowing stream used in this study quickly removes evolved HCl, the back reaction between HCl and $NaNO_3$ can be neglected. Thus, the effective rate constant, k_{eff}, can be described by the following relationship:

$$k_{\mathrm{eff}} = \frac{k_1 k_2}{k_{-1} + k_2} \tag{6}$$

Previous studies provide insight into the steps that govern this reaction and aid in the determination of the rate-limiting step in this process. Fenter et al. observed rapid uptake of HNO_3 and a delay in HCl release.[17] When HNO_3 flow was stopped, 90−95% of the HNO_3 desorbed, indicating that k_{-1} is larger than k_2.[17] These observations suggest that HNO_3 adsorption is facile and HCl formation is limited by reaction 5. Assuming that the HNO_3 adsorption equilibrium is rapidly established, eq 6 simplifies to

$$k_{\mathrm{eff}} = \frac{k_1}{k_{-1}} k_2 = k_{\mathrm{eq}} k_2 \tag{7}$$

Assuming little dependence of HNO_3 (k_{eq}) on surface preparation, the rate of reaction 5, k_2, is most likely related to the active site density of the surface.

Although the exact chemical nature of these active sites is unknown, they most likely involve surface H_2O. Furthermore, these sites must be continually regenerated for the surface reaction to continue. AFM measurements suggest that the surface reactivity is greatest at step edges;[19] thus, these step edges are surmised to be the region of the surface with the highest density of active sites. Once reaction 5 has occurred at an active site, the formation of surface $NaNO_3$ results in reconstruction of the surface to accommodate the replacement of Cl^- by the sterically larger NO_3^-. This reconstruction is thought to continually regenerate new active sites until the passivating layer is complete.

Effect of H_2O Exposure on the $NaNO_3$-Passivated Surface. Previous studies on this reaction have shown a significant rearrangement of the amorphous $NaNO_3$ layer upon exposure to H_2O.[14−17,19] The effect of H_2O vapor on $NaNO_3$-capped NaCl was studied here with Raman spectroscopy. Upon exposure of the $NaNO_3$-capped surface to H_2O vapor at 1×10^{-5} moles of H_2O s^{-1}, a second $\nu_s(NO_3^-)$ band appears at 1052 cm^{-1} as shown in the spectrum in Figure 7b; this band is assigned to the $\nu_s(NO_3^-)$ mode of solution-phase NO_3^-. This band first becomes visible upon exposure of the powder to $\sim 8 \times 10^{-7}$ moles of H_2O cm^{-2} and increases in intensity with H_2O exposure. After exposure to 3×10^{-6} moles of H_2O cm^{-2}, the spectrum in Figure 7c is observed which is consistent with a saturated aqueous solution of $NaNO_3$.

Previous work has shown that the frequency of the $\nu_s(NO_3^-)$ mode of aqueous solution $NaNO_3$ is concentration-dependent.[25] In saturated aqueous solutions (~6 M $NaNO_3$), this mode appears at 1052 cm^{-1} but shifts to lower frequencies with decreasing concentration (e.g., 1049 cm^{-1} at ~0.5 M $NaNO_3$.)[25] The invariant frequency of the solution $\nu_s(NO_3^-)$ mode on NaCl with increasing H_2O exposure is consistent with a thin H_2O film that remains saturated with $NaNO_3$ for all exposures up to 3.6×10^{-6} moles of H_2O cm^{-2}. Using minimum hydration numbers of 5 and 6 for NO_3^- and Na^+, respectively,[26,27] and assuming an ~10 Å $NaNO_3$ passivating layer[14−16] of bulk $NaNO_3$ density, a H_2O layer thickness of ~25 Å is estimated for minimum hydration of all $NaNO_3$ in the passivating layer.

Dissolution of $NaNO_3$ on the NaCl surface is reversible, as shown by the spectrum in Figure 7d. This spectrum was acquired on the same sample that gave the spectrum in Figure 7c after flowing dry air (RH < 2%) through it. The re-emergence of the solid-state $\nu_s(NO_3^-)$ band at 1068 cm^{-1} after exposure to $\sim 2 \times 10^3$ equivalent cell volumes of dry air indicates the precipitation of $NaNO_3$ from the thin H_2O layer as H_2O is removed. Interestingly, loss of the 1052 cm^{-1} band is not complete even after 12 h of dry air flow through the powder. This observation is consistent with previous work that has shown that complete removal of surface H_2O from NaCl requires temperatures above 350 °C.[28]

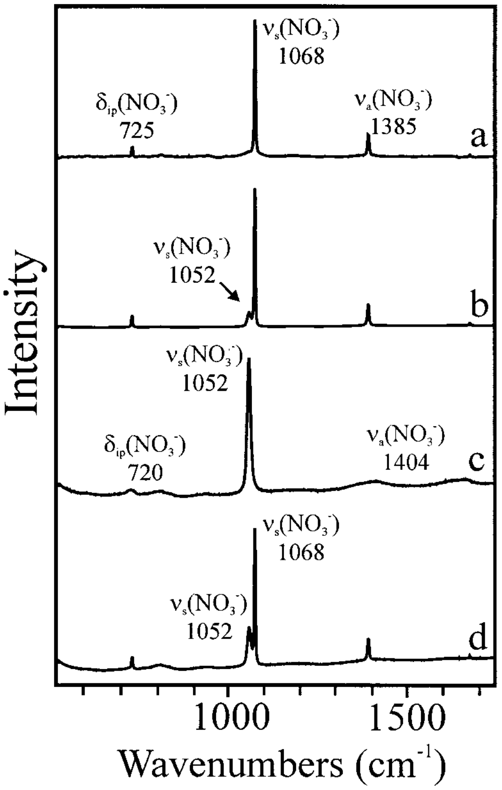

Figure 7. Raman spectra upon the exposure of $NaNO_3$-capped NaCl to H_2O. (a) Spectrum prior to H_2O exposure; spectra after exposure to (b) $\sim 8 \times 10^{-7}$ and (c) $\sim 3 \times 10^{-6}$ moles of H_2O cm^{-2}, and (d) the powder from panel c to dry air (RH ~2%) for 7 min.

This H_2O removal process also results in changes in the nature of the solid-state $NaNO_3$ on the NaCl surface. The intensity ratio of the $\nu_s(NO_3^-)$ to $\delta_{ip}(NO_3^-)$ modes decreases from the 15:1 value characteristic of the fully formed amorphous passivating layer to the crystalline $NaNO_3$ value of 12:1. This observation is consistent with previous XPS[14−16] and AFM[19] work showing that surface hydration results in a precipitation-based growth of rhombohedral $NaNO_3$ crystals from amorphous $NaNO_3$ on NaCl (100).

The involvement of surface-adsorbed H_2O in the transformation of the amorphous $NaNO_3$ layer to crystalline $NaNO_3$ was further investigated by monitoring the ν(O−H) region as a function of H_2O exposure. Spectral results are shown in Figure 8. No detectable H_2O was observed prior to H_2O exposure, as shown in Figure 8a. Exposure of $NaNO_3$-capped NaCl to 2×10^{-6} moles of H_2O cm^{-2} produces the spectrum shown in Figure 8b, with ν(O−H) bands from H_2O clearly evident. This spectrum corresponds to the surface state of NO_3^- indicated by spectrum Figure 7b, in which both dissolved NO_3^- and solid-state $NaNO_3$ coexist on the NaCl surface.

The intensity in the ν(O−H) region continues to increase with additional H_2O exposure, indicating an increased thickness of the surface adsorbed H_2O layer, Figure 8c. This spectrum corresponds to the NO_3^- state shown in Figure 7c, in which all NO_3^- is dissolved. It should be noted that the visual appearance

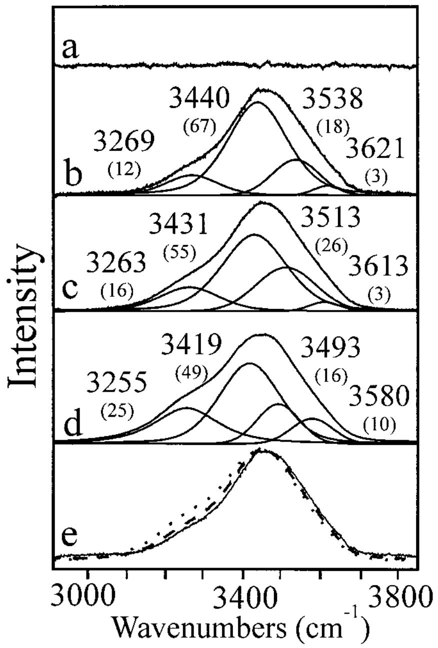

Figure 8. Raman spectra in ν(O−H) region upon the exposure of $NaNO_3$-capped NaCl to H_2O. (a) Spectrum prior to H_2O exposure; spectra after exposure to (b) ~2×10^{-6} and (c) ~3×10^{-6} moles of H_2O cm^{-2}; (d) spectrum of aqueous solution saturated in NaCl and $NaNO_3$; (e) overlaid spectra from panels b (solid line), c (dashed line), and d (dotted line). Peak fits for four components shown below each spectrum.

of the NaCl powder with this amount of surface H_2O is such that it still appears solid, although some caking of the powder is now evident.

It is interesting to compare the spectra of the ν(O−H) region in Figure 8b,c with that of an aqueous solution saturated in both NaCl and $NaNO_3$ in Figure 8d. Although these spectra are similar, they are not identical (see overlaid spectra in Figure 8e), which clearly indicates the unique nature of the ultrathin H_2O layer existing on the NaCl surface in this system. A better understanding of differences between these spectra can be achieved by a more detailed analysis of the spectral components contained within the ν(O−H) envelope.

The complex shape of the ν(O−H) envelope has given rise to multiple interpretations and has been studied with Raman spectroscopy for over 30 years.[27−35] This region is mainly composed of ν_s(OH) modes from ~3440−3600 cm^{-1}; a weak contribution from the ν_a(OH) is also observed at frequencies greater than 3630 cm^{-1} in pure H_2O. The peak frequencies and relative intensities provide insight into the hydrogen bonding environment and degree of order within the H_2O film. In pure H_2O, this envelope can be fit with four components[30,35] that have been attributed to an ice-like component (C_1) at 3230 cm^{-1}, an ice-like liquid phase (C_2) at 3420 cm^{-1}, a liquidlike amorphous phase (C_3) at 3540 cm^{-1}, and monomeric H_2O (C_4) at 3620 cm^{-1}.[30]

The addition of certain ions disrupts hydrogen bonding, thereby increasing the intensities of the amorphous and monomer components (C_3 and C_4, respectively) relative to their intensities in pure H_2O. The intensity ratio of the C_1 mode to the C_2 mode is also sensitive to the extent of hydrogen bonding in solution. For example, the ratio in pure H_2O is ~1. However, the presence of certain structure-breaking ions disrupts hydrogen bonding,[26,27,36] resulting in a C_1:C_2 ratio reduced to ~0.5.[30]

TABLE 1: Peak Positions for ν(O−H) Modes of Surface Bound H_2O and Bulk Aqueous Solutions. Peak Areas Are Shown in Parentheses

	component			
	C_1	C_2	C_3	C_4
$NaNO_3$-capped NaCl	3269	3440	3538	3621
(2×10^{-6} moles of H_2O cm^{-2})	(12)	(67)	(18)	(3)
$NaNO_3$-capped NaCl	3263	3431	3513	3613
(3×10^{-6} moles of H_2O cm^{-2})	(16)	(49)	(26)	(3)
saturated NaCl + $NaNO_3$	3255	3419	3493	3580
	(25)	(49)	(16)	(10)
saturated NaCl	3244	3394	3476	3588
	(19)	(41)	(31)	(9)
saturated $NaNO_3$	3256	3404	3496	3586
	(21)	(46)	(23)	(11)

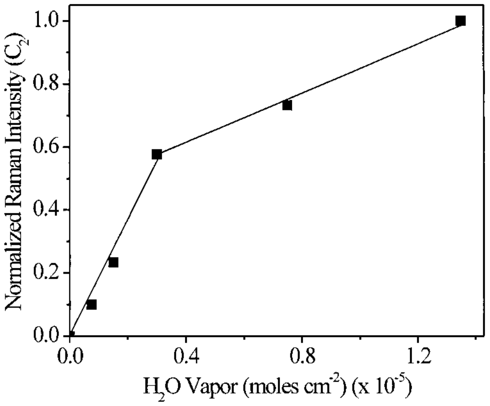

Figure 9. Normalized integrated intensity of the C_2 component of ν(O−H) Raman spectral envelope as a function of H_2O exposure.

The peak frequency and integrated intensity data for the spectra in Figure 8 and from single-component saturated solutions of NaCl and $NaNO_3$ (spectra not displayed) are shown in Table 1. Several observations about these data are noteworthy. First, as the amount of surface-adsorbed H_2O increases, all four components shift to lower frequency. Second, the C_1:C_2 intensity ratio increases with H_2O exposure, while the C_4 component is unchanged and ~70% lower than observed for an aqueous solution saturated in both NaCl and $NaNO_3$. These changes are all consistent with an increase in hydrogen bonding character within the thin H_2O film with increasing amount.

The integrated intensity of the C_2 component as a function of H_2O exposure is shown in Figure 9. The C_2 component has the largest integrated intensity, and over a broad concentration range, is nearly invariant in intensity. The change in the slope of the C_2 component at ~3×10^{-6} moles of H_2O cm^{-2} occurs at the H_2O exposure at which all of the solid $NaNO_3$ dissolves in the surface adsorbed water layer (Figures 7c and 8c.) This decrease in H_2O uptake by the surface at the point of total amorphous $NaNO_3$ dissolution is consistent with the metastability of this amorphous layer.

In reality, the NaCl surface will never be dehydrated as it is in the starting point of this and previous studies. Under most conditions in the atmosphere, NaCl is formed through flash evaporation of a small liquid aerosol droplet as it encounters regions of lower relative humidity. Temperatures required for complete H_2O removal from NaCl are not achieved in the terrestrial atmosphere.[28] Thus, formation of particulate NaCl from aqueous droplets leads to surface-bound H_2O under conditions of RH well below the NaCl deliquescence point (DP) (RH < 74%), and complete three-dimensional H_2O coverage, with time-dependent continuing condensation of H_2O, at RH values greater than the DP.

Therefore, to model NaCl surface processes that occur in the terrestrial atmosphere, H_2O must be added to the surface.

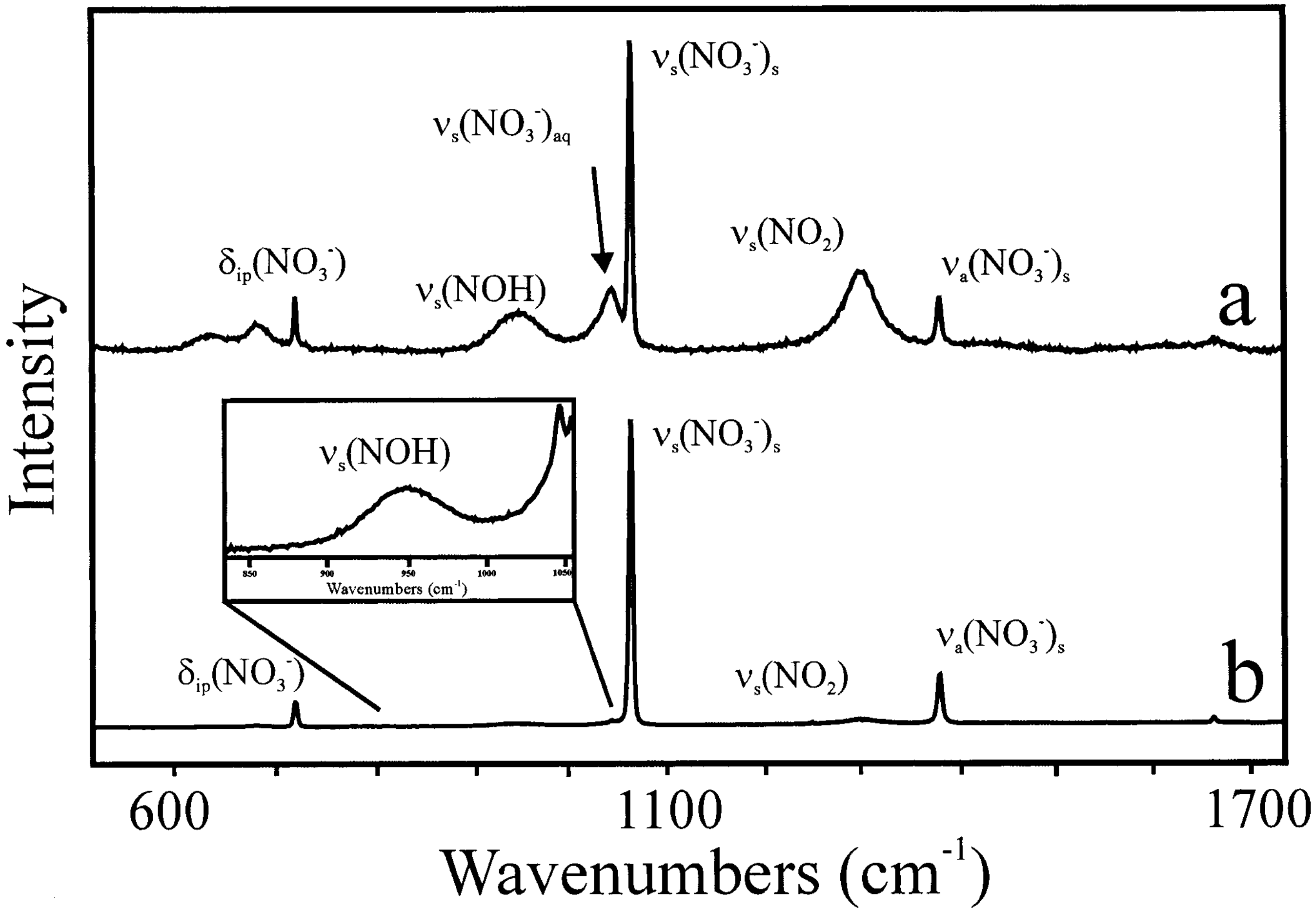

Figure 10. Raman spectra upon the exposure of deliquesced NaCl powder (exposure ~1 × 10^{-4} moles of H_2O cm^{-2}) to (a) ~5 × 10^{-6} and (b) ~5 × 10^{-5} moles of HNO_3 cm^{-2}.

Toward this end, we have studied the reaction of NaCl with HNO_3 at a prehydrated NaCl surface. Such conditions were simulated by producing a well-hydrated surface with a substantial H_2O layer (total exposure of 1 × 10^{-4} moles of H_2O cm^{-2}). This surface was then exposed to a flowing stream of dry HNO_3 vapor, and Raman spectra were monitored as a function of time. Exposure of prehydrated NaCl to 4.2 × 10^{-7} moles of HNO_3 cm^{-2} produces the spectrum of predominately solid-state $NaNO_3$ shown in Figure 10a. However, several additional bands are observed that are can be attributed to molecular HNO_3: the δ(ONO) at 620−670 cm^{-1}, the ν_s(NOH) at 930 cm^{-1}, and the $\nu_s(NO_2)$ at 1310 cm^{-1}.[37] Deprotonation of HNO_3 results in a change in symmetry from C_{2v} for HNO_3 to D_{3h} for NO_3^-. Therefore, the Raman spectrum of free NO_3^- is dominated by the $\nu_s(NO_3^-)$ at 1046 cm^{-1}.[37] Thus, the band at 1049 cm^{-1} can be attributed to NO_3^- from either dissolved $NaNO_3$, deprotonated HNO_3, or both.

HNO_3 is a strong acid that is readily ionized in the presence of H_2O. Irish et al. showed that in the absence of other electrolytes in solution, HNO_3 is 17% ionized with 1.5 H_2O molecules per HNO_3 and 63% ionized with 5 H_2O molecules per HNO_3.[37] In the presence of other electrolyte ions, which compete with the proton for hydration, the deprotonation process is inhibited. The extent of HNO_3 deprotonation depends on the number of H_2O molecules available for hydration. Obviously, the number of H_2O molecules on the NaCl surface in this thin film is limited by the H_2O exposure. The presence of molecular HNO_3 spectral bands suggests that the number of H_2O available to hydrate a dissociating proton is most likely not many more than 5 per HNO_3 and must be less than 12 per HNO_3, the number at which very little molecular HNO_3 exists in solution.[37] Furthermore, the NaCl surface H_2O is assumed to be saturated in NaCl prior to HNO_3 exposure. Thus, the HNO_3 must compete for H_2O for deprotonation with Na^+ and Cl^- hydration. Assuming complete uptake of the HNO_3 by the surface and recognizing that the amount of surface H_2O is small, this thin H_2O layer is expected to be quite acidic despite incomplete HNO_3 dissociation. As shown by Clegg et al., the acidity of a surface H_2O layer would promote degassing of the HCl produced in the reaction of HNO_3 with the NaCl surface,[38,39] driving this reaction to the right.

Finally, as shown by the spectrum in Figure 10b, the intensity of the solid-state $NaNO_3$ modes increases with additional HNO_3 exposure. However, spectral evidence for the existence of molecular HNO_3 (inset in Figure 10b) is still observed after exposure of the prehydrated NaCl surface to 4.2 × 10^{-6} moles of HNO_3 cm^{-2} (1 order of magnitude more than the exposure in Figure 10a).

$NaNO_3$ precipitates at concentrations above 6.9 M in a solution saturated in both $NaNO_3$ and NaCl.[40] If a HNO_3 uptake coefficient of unity is assumed, the aqueous layer would be saturated in $NaNO_3$ in ~0.5 s, a time faster than can be explored with our Raman spectroscopy experiment. Thus, the existence of exclusively a solution NO_3^- layer on the NaCl surface cannot be ascertained with the current experimental arrangement.

Conclusions

Raman spectral results for the reaction of dry HNO_3 with NaCl surfaces confirm the previously observed[14−16,19] initial formation of an amorphous passivating layer of $NaNO_3$. The intensity ratio of two prominent Raman-active modes, the $\nu_s(NO_3^-)$ and the $\delta_{ip}(NO_3^-)$, for this amorphous layer is significantly different from that of bulk crystalline $NaNO_3$ and is a function of surface coverage. The $\nu_s(NO_3^-)$ mode intensity can be fit to a simple Langmuir isotherm, which suggests that the first step in this process is simple adsorption. Force field energy minimization calculations indicate reorientation of the NO_3^- species in this layer as it forms. The results of these calculations also predict an amorphous layer product due to the lattice mismatch between the $NaNO_3$ product and the NaCl surface.

The rate constant for amorphous layer formation and the corresponding reaction probability, γ, for this reaction have been determined for the first time from Raman spectral data. The γ value of 5.9×10^{-2} determined here for NaCl powders is similar to although slightly higher than previous estimates based on monitoring gas-phase products. The expected accuracy of this value determined from monitoring the solid-state product instead of the gas-phase product is noted.

H_2O-induced reorganization of this amorphous $NaNO_3$ layer by Raman spectroscopy clearly indicates the involvement of a thin H_2O layer, as previously hypothesized.[14−16] Indeed, direct evidence for the presence of this layer can be observed in the ν(O−H) region of the vibrational spectrum. A detailed analysis of this spectral response suggests a unique environment that is not modeled by aqueous solution saturated with NaCl and $NaNO_3$. On the basis of spectral evidence of dissolved NO_3^- species, the growth of rhombohedral $NaNO_3$ crystals as previously observed[15,19] most likely occurs by a precipitation-based mechanism.

Acknowledgment. The authors gratefully acknowledge support of this research by the National Science Foundation (CHE-0075813).

References and Notes

(1) Graedel, T. E.; Keene, W. C. *Global Biogeochem. Cycles* **1995**, *9*, 47.

(2) DeMore, W. B.; Sandler, S. P.; Golden, D. M.; Hampson, R. F.; Kurylo, M. J.; Howard, C. J.; Ravishankara, A. R.; Kolb, C. E.; Molina, M. J. *Chemical Kinetics and Photochemical Data for Use in Stratospheric Modeling*; Evaluation No. 12, JPL Publ. No. 97-4; Jet Propulsion Laboratory: Pasadena, CA, 1997.

(3) Peters, S. J.; Ewing, G. E. *J. Phys. Chem.* **1996**, *100*, 14093.

(4) Harkel, M. J. *Atmos. Environ.* **1997**, *31*, 417.

(5) Kleeman, M. J.; Hughes, L. S.; Allen, J. O.; Cass, G. R. *Environ. Sci. Technol.* **1999**, *33*, 4331.

(6) Karlsson, R.; Ljungstrom, E. *J. Aerosol Sci.* **1995**, *26*, 39.

(7) Gard, E.; Kleeman, M. J.; Gross, D. S.; Hughes, L. S.; Allen, J. O.; Morrical, B. D.; Fergenson, D. P.; Dienes, T.; Galli, M. E.; Johnson, R. J.; Cass, G. R.; Prather, K. A. *Science* **1998**, *279*, 1184.

(8) Vogt, R.; Finlayson-Pitts, B. J. *J. Phys. Chem.* **1994**, *98*, 3747.

(9) Langer, S.; Pemberton, R. S.; Finlayson-Pitts, B. J. *J. Phys. Chem. A* **1998**, *101*, 1277.

(10) Leu, M.; Timonen, R. S.; Keyser, L. F.; Yung, Y. L. *J. Phys. Chem.* **1995**, *99*, 13203.

(11) Biechert, P.; Finlayson-Pitts, B. J. *J. Phys. Chem.* **1996**, *100*, 15218.

(12) Davies, J. A.; Cox, R. A. *J. Phys. Chem. A* **1998**, *102*, 7631.

(13) Abbatt, J. P. D.; Waschewsky, G. C. G. *J. Phys. Chem. A* **1998**, *102*, 3719.

(14) Laux, J. M.; Fister, T. F.; Finlayson-Pitts, B. J.; Hemminger, J. C. *J. Phys. Chem.* **1996**, *100*, 19891.

(15) Allen, H. C.; Laux, J. M.; Vogt, R.; Finlayson-Pitts, B. J.; Hemminger, J. C. *J. Phys. Chem.* **1996**, *100*, 6371.

(16) Ghosal, S.; Hemminger, J. C. *J. Phys. Chem. A* **1999**, *103*, 4777.

(17) Fenter, F. F.; Caloz, F.; Rossi, M. J. *J. Phys. Chem.* **1994**, *98*, 9801.

(18) Seinfeld, J. H.; Pandis, S. N. *Atmospheric Chemistry and Physics: From Air Pollution to Climate Change*; John Wiley and Sons: New York, 1998.

(19) Zangmeister, C. D.; Pemberton, J. E. *J. Phys. Chem. B* **1998**, *102*, 8950.

(20) Sunagawa, I.; Tsukamoto, K. *J. Crystal Growth* **1972**, *15*, 73.

(21) Knoppik, D.; Lsch, A. *J. Crystal Growth* **1976**, *34*, 332.

(22) Hari Babu, V.; Bansigir, K. G. *J. Crystal Growth* **1970**, *6*, 192.

(23) Mayo, S. C.; Olafson, B. D.; Goddard, W. A. *J. Phys. Chem.* **1990**, *94*, 88971.

(24) Edelwirth, M.; Freund, J.; Sowerby, S. J.; Heckl, W. M. *Surface Sci.* **1998**, *417*, 201.

(25) Irish, D. E.; Davis, A. R. *Can. J. Chem.* **1968**, *46*, 943.

(26) Kameda, Y.; Saitoh, H.; Uemura, O. *Bull. Chem. Soc. Jpn.* **1993**, *66*, 1919.

(27) Kameda, Y.; Sugawara, K.; Usuki, T.; Uemura, O. *Bull. Chem. Soc. Jpn.* **1998**, *71*, 2729.

(28) Barraclough, P. B.; Hall, P. G. *Surf. Sci.* **1974**, *46*, 393.

(29) Walrafen, G. E. *J. Chem. Phys.* **1962**, *36*, 1035.

(30) Walrafen, G. E. *J. Chem. Phys.* **1970**, *52*, 4176.

(31) Walrafen, G. E. *J. Chem. Phys.* **1971**, *55*, 768.

(32) Luu, D. V.; Cambon, L.; Mathlouthi, M. *J. Mol. Struct.* **1990**, *237*, 411.

(33) Maeda, Y.; Tsukida, N.; Kitano, H.; Terada, T.; Yamanaka, J. *J. Phys. Chem.* **1993**, *97*, 13903.

(34) Yoshimura, Y.; Kanno, H. *J. Raman Spec.* **1996**, *27*, 671.

(35) Carey, D. M.; Korenowski, G. M. *J. Chem. Phys.* **1998**, *108*, 2669.

(36) Driesner, T.; Seward, T. M.; Tironi, I. G. *Geochim. Cosmochim. Acta* **1998**, *62*, 3095.

(37) Ratcliffe, C. I.; Irish, D. E. *Can. J. Chem.* **1985**, *63*, 3521.

(38) Clegg, S. L.; Brimblecombe, P. *Atmos. Environ.* **1988**, *22*, 91.

(39) Brimblecombe, P.; Clegg, S. L. *Atmos. Environ.* **1988**, *7*, 1.

(40) Silcock, H. L. *Solubilities of Inorganic and Organic Compounds, Vol. 3. Ternary and Multicomponent Systems of Inorganic Substances, Part 2.*; Pergamon Press: New York, 1978.